INORGANIC CHEMISTRY FRONTIERS

RESEARCH ARTICLE

View Article Online
View Journal | View Issue

Cite this: *Inorg. Chem. Front.*, 2023, **10**, 804

B-site substitution in $NaCo_{1-2x}Fe_xNi_xF_3$ perovskites for efficient oxygen evolution†

Hu Yao,[a] Yinan Zheng,[a] Siliang Yue,[a] Songjie Hu,[a] Wenyu Yuan*[b] and Xiaohui Guo *[a]

Received 24th October 2022,
Accepted 29th November 2022

DOI: 10.1039/d2qi02275c

rsc.li/frontiers-inorganic

The oxygen evolution reaction (OER) has slow chemical dynamics in the electrochemical decomposition of water. Herein, we demonstrate that B-site substitution engineering on ABF_3 is an efficient strategy to boost the OER activity due to the modified electronic structure. A series of perovskite fluorides with the formula $NaCo_{1-2x}Fe_xNi_xF_3$ were fabricated *via* a simple hydrothermal process, in which Co was partially substituted by both Fe and Ni. The optimized perovskite fluoride exhibited a low overpotential of 265 mV at a current density of 10 mA cm^{-2} and outstanding electrochemical stability after 100 h continuous electrocatalysis for the OER. These results are superior to the state-of-the-art perovskite-based OER catalysts. The X-ray photoelectron spectroscopy (XPS) and X-ray absorption fine structure (XAFS) results showed that the dual-substitution of Fe and Ni atoms not only produced higher valence Co^{3+} ions but also generated the more active species Fe^{3+}. In addition, the produced metal oxyhydroxides (MOOH, M = Co, Fe, Ni) on the catalyst surface during OER activation could contribute both excellent catalytic activity and ultralong stability.

1. Introduction

Oxygen evolution reaction (OER) is a critical half-cell reaction in rechargeable metal–air batteries and water splitting. Due to the OER involving a four-electron transfer path, it suffers from sluggish kinetics, resulting in a high overpotential in practice. Thus, electrocatalysts with high activity are desired to enhance the overall efficiency of these energy-conversion devices.[1–6] Although noble metal oxides (*e.g.* IrO_2 and RuO_2) are considered as high-activity catalysts, their typical high cost and severe scarcity have restricted their large-scale application.[7] Therefore, there is a crucial need to develop advanced OER catalysts with high-activity, low cost, and high stability.

For this purpose, numerous research efforts have focused on catalysts based on the first-row transition metals as viable alternatives for the OER,[8–10] including their transition-metal sulfides,[11] nitrides,[12] oxides,[13,14] and (oxy)-hydroxides.[15] Among these electrocatalysts, perovskite oxides (ABO_3) with an ordered atomic arrangement and highly flexible electronic structure[16–19] have attracted tremendous attention, where A is an alkali metal and B is a transition metal (Ti, Mn, Fe, Co, Ni, *etc.*). The B-sites of perovskites can be easily substituted by atoms with similar atomic radii for structural and electronic regulation, which can easily modulate the catalytic properties of perovskites.[20] For example, Sun *et al.*[21] replaced Co in the B-site of $LaCoO_3$ perovskite with Mn, which could modulate the e_g electron filling and O 2p–Co 3d covalency, thereby improving the overall catalytic activity for the OER. Similarly, Duan *et al.*[22] found that an overlap between the O 2p and Co 3d states occurred in $LaCo_{0.9}Fe_{0.1}O_3$, which led to an optimal e_g conformation and enhanced covalency, and improved catalytic activity for the OER. Ede *et al.*[23] optimized the OER activity of Sr–Co–Fe–O by changing the Co/Fe ratio, which proved that the excellent activity could be attributed to its layered anoxic structure and the increased Co 3d and O 2p covalence. Liu *et al.*[24] designed mixed valences of Co^{2+}/Co^{3+} and Mn^{3+}/Mn^{4+} and abundant oxygen vacancies in $LaMnO_3$ perovskites by replacing Mn in part with Co to achieve a higher bi-functional activity. These results revealed that the partial substitution of the B-site cation in the perovskite by highly reactive metal elements can tune many properties of perovskites, such as changing the oxygen vacancies, electronic structure, bond strength, and synergistic interactions.

Due to the strongest electronegativity of the fluorine (F) anion, F is an ideal n-type dopant, which enables the formation of weak M–F bonds and strong ionicity. Thus, perovskite fluorides are promising candidates to achieve enhanced

[a]*Key Lab of Synthetic and Natural Functional Molecule Chemistry of Ministry of Education, The College of Chemistry and Materials Science, Northwest University, Xi'an 710069, P. R. China. E-mail: guoxh2009@nwu.edu.cn*
[b]*Key Laboratory of Macromolecular Science of Shaanxi Province, Key Laboratory of Applied Surface and Colloid Chemistry, School of Chemistry & Chemical Engineering, Shaanxi Normal University, Xi'an 710062, P. R. China*
† Electronic supplementary information (ESI) available. See DOI: https://doi.org/10.1039/d2qi02275c

OER activity compared with ABO_3.[25,26] Chandrappa *et al.* first reported the fluoride perovskite series $KNi_xCo_{1-x}F_3$ as promising OER catalysts.[26] However, to the best of our knowledge, the bimetallic substitution and the effects of B-site substitution for perovskite fluorides on the OER activity have not been systematically explored up to now.

Based on the above consideration, B-site substitution engineering *via* using bimetals on ABF_3 was investigated and consequently a series of $NaCo_{1-2x}Fe_xNi_xF_3$ catalysts were successfully synthesized for the first time. The prepared $NaCo_{0.4}Fe_{0.3}Ni_{0.3}F_3$ (NCFNF(433)) delivered a small overpotential of 265 mV at 10 mA cm^{-2} current density, a low Tafel slope of 49 mV dec^{-1}, and excellent electrochemical stability during 100 h of continuous electrocatalysis. The experimental results showed that the active centres in NCFNF(433) were Co and Fe species, and Ni acted as an acceptor of electrons from Co and Fe. The catalytic performance was further improved by changing the charge distribution of Co and Fe to produce highly active species. These results strongly showed that NCFNF(433) is a durable, efficient, and economical OER electrocatalyst. This work provides new insights into the potential of substitution engineering design for developing advanced perovskite-based catalysts for use in the energy-conversion field.

2. Experimental section

2.1 Preparation of $NaCo_{1-2x}Fe_xNi_xF_3$ perovskite materials

All the chemical reagents were used without further purification. The $NaCo_{1-2x}Fe_xNi_xF_3$ powders were prepared *via* a facile modified solvothermal process. The typical synthetic process was as follows: first, 0.1993 g of $Co(OAc)_2{\cdot}4H_2O$, 0.2353 g of $Fe(NH_4)_2(SO_4)_2{\cdot}6H_2O$, 0.1493 g of $Ni(OAc)_2{\cdot}4H_2O$, 0.1558 g of sodium citrate dihydrate, and 0.3182 g of NH_4F were added to a mixed solvent of water and ethylene glycol $(CH_2OH)_2$ (1 mL : 16 mL) and magnetically stirred to give a homogeneous solution, and then the solution was further processed in an ultrasonic bath. Next, the resulting solution was heated at 200 °C for 12 h in a 20 mL Teflon autoclave. After the autoclave had cooled to room temperature (25 °C), the resulting precipitates were collected by centrifugation at 8000 rpm for 3 min and washed with distilled water and absolute ethanol 3 times. Finally, the product was dried at 70 °C overnight to obtain the final samples. The synthetic method for $NaCo_{1-2x}Fe_xNi_xF_3$ (x = 0/0.1/0.2/0.3) was the same as for NCFNF(433), except for the ratio of Co, Fe, and Ni slats and the products were denoted as NCF, NCFNF(811), NCFNF(622), and NCFNF(433). Additionally, $NaCo_{0.7}Ni_{0.3}F_3$ and $NaCo_{0.7}Fe_{0.3}F_3$ were denoted as NCNF(73) and NCFF(73), respectively.

2.2 Material characterization

Powder X-ray diffraction (XRD) pattern of $NaCo_{1-2x}Fe_xNi_xF_3$ was collected using a Bruker D8 Advance X-ray diffractometer (Cu Kα radiation) at a scanning rate of 0.05° s^{-1}. The morphology and structure of the $NaCo_{1-2x}Fe_xNi_xF_3$ perovskite sample were analyzed by scanning electron microscopy (SEM, SU-8010) and transmission electron microscopy (FEI, Talos-200). EDS mapping was used to measure the element distribution and composition of $NaCo_{1-2x}Fe_xNi_xF_3$. The surface elemental distribution and chemical states were determined by X-ray photoelectron spectroscopy (XPS, Thermo Scientific, ESCALAB Xi^+) with an Al Kα X-ray source. Raman spectroscopy was performed with a confocal Raman microspectroscope (Jobin Yvon Co., France, HR800) in the range of 200–3000 cm^{-1} using a 532 nm laser. The chemical bonds of the samples were investigated by Fourier transform infrared spectroscopy (FT-IR) (Nicolet 6700, Thermo Fisher). The source for obtaining the X-ray absorption near-edge spectra data was the Beijing Synchrotron Radiation Facility.

2.3 Electrochemical measurements

The electrochemical performance of the OER was evaluated using a three-electrode system on the CHI760E electrochemical station, with Hg/HgO (1 M KOH) used as the reference electrode, while the counter and the working electrodes were Pt foil and the glass carbon RDE (3 mm in diameter; area: 0.0707 cm^2), respectively. All the measured potentials *vs.* Hg/HgO were converted to the reversible hydrogen electrode (RHE). In 1 M KOH, $E_{RHE} = 0.0977\ V + 0.059 \times pH + E_{Hg/HgO}$. The working electrode was prepared as follows: first, 5 mg of catalysts, 1 mg of carbon black, and 50 μL of Nafion (5 wt%) were evenly dispersed in the mixture solution together with 950 μL ethanol. Then, 5 μL of the liquid obtained in the previous step was added to a glassy carbon electrode with a surface area of 0.0707 cm^2, and the electrode was dried at room temperature. The catalyst load on the electrode was about 0.35 mg cm^{-2}. A commercial RuO_2 catalyst obtained from Aladdin was used for comparison. The activation of the working electrodes and OER performance were tested by cyclic voltammetry (CV) and linear sweep voltammetry (LSV) (scan rates of 50 and 5 mV s^{-1}, respectively). The electrochemical impedance spectrum (EIS) of the catalyst was tested at a potential of 1.524 V *vs.* RHE (amplitude 5 mV) in 1 M KOH solution over a frequency range of 100 mHz to 100 kHz. The turnover frequency (TOF) was calculated by the following equation:

$$\mathrm{TOF}\ (s^{-1}) = j \times A/(4F \times n)$$

where j (A cm^{-2}) is the current density at an overpotential of 300 mV, A is the surface area of the glassy carbon electrode, F is the Faraday constant (96 500 C mol^{-1}), and n (mol) is the number of moles of catalyst loaded onto the working electrode.

The electrochemically active surface area (ECSA) was determined by measuring the CV scan rate dependence with respect to the capacitive current associated with the double-layer charging. The potential window of CV was set to be 1.34–1.44 V *vs.* RHE and the scan rates were 10, 30, 50, 70, 90, and 110 mV s^{-1}. The double-layer capacitance (C_{dl}) was tested by plotting $\Delta j = (j_+ - j_-)/2$ at 1.39 V *vs.* RHE against the scan rate. The ECSA was evaluated by the following equation:

$$\mathrm{ECSA} = C_{dl}/0.04\ \mathrm{mF\ cm^{-2}\ per\ cm^2}.$$

For long-term stability testing, the catalyst was dropped onto carbon paper (area: 1 × 1 cm^2; mass loading: 0.35 mg cm^{-2}). The loading mass of the RuO_2 on carbon cloth was about 0.35 mg cm^{-2}, which was similar to our $NaCo_{1-2x}Fe_xNi_xF_3$ electrocatalysts.

3. Results and discussion

The typical perovskite fluorides were synthesized by a facile one-step hydrothermal method. The Fe and Ni metal ions were chosen as metal sources for the B-site engineering on ABF_3 because of their high catalytic activity and similar ionic radius. Fig. S1† displays the crystallographic unit cell of the $NaCo_{1-2x}Fe_xNi_xF_3$ perovskite fluorides, in which the transition metal ions (Co/Fe/Ni) on the B-sites reside in corner-sharing octahedra of F anions, while the A-site cations (Na) have 8-fold coordination with F.[27,28] X-ray powder diffraction (XRD) patterns suggested that the as-synthesized $NaCo_{1-2x}Fe_xNi_xF_3$ exhibited a pure perovskite phase without other impurities. Taking NCFNF(433) as a representative, all the diffraction peaks matches were in good agreement with the standard ICDD card no. 04-008-3556. The detected peaks at 22.78°, 32.46°, 46.53°, 52.43°, and 57.57° were assigned to the (101), (121), (112), (202), (222), and (240) planes, respectively (Fig. 1a). As the content of Fe and Ni in $NaCo_{1-2x}Fe_xNi_xF_3$ increased from 0 to 0.3, the main diffraction peak (101) showed a gradual shift to the right (large angles) (Fig. 1b). This change showed there was a regular change in the lattice of $NaCo_{1-2x}Fe_xNi_xF_3$ due to the partial introduction of Fe and Ni, a typically solid solution characteristic of the perovskite structure. Compared to NCF, the diffraction peaks of NCFNF (433) shifted from 22.78° to 22.96°, which provided direct evidence for the successful substitution.[29,30] The morphology and size of the perovskite fluorides $NaCo_{1-2x}Fe_xNi_xF_3$ were observed by scanning electron microscopy (SEM). The SEM images of $NaCo_{1-2x}Fe_xNi_xF_3$ revealed a stacked nanocrystalline morphology (Fig. S2–S5†). Both the degree of agglomeration and the sizes of the particles decreased with the substitution of Fe and Ni.

High-resolution transmission electron microscopy (HRTEM) images and corresponding selected area electron diffraction (SAED) further confirmed the obtained structure (Fig. 1c and d). The HRTEM images in Fig. 1c and Fig. S6a–c† displayed clear lattice stripes, which were assigned to the (101) diffraction planes of $NaCo_{1-2x}Fe_xNi_xF_3$, showing lattice spacings of 3.89, 3.84, 3.81, and 3.78 Å, respectively. The decreased lattice distance for $NaCo_{1-2x}Fe_xNi_xF_3$ was also in agreement with the crystal structural disorder and lattice shrinking in XRD, which was due to introducing Fe and Ni in

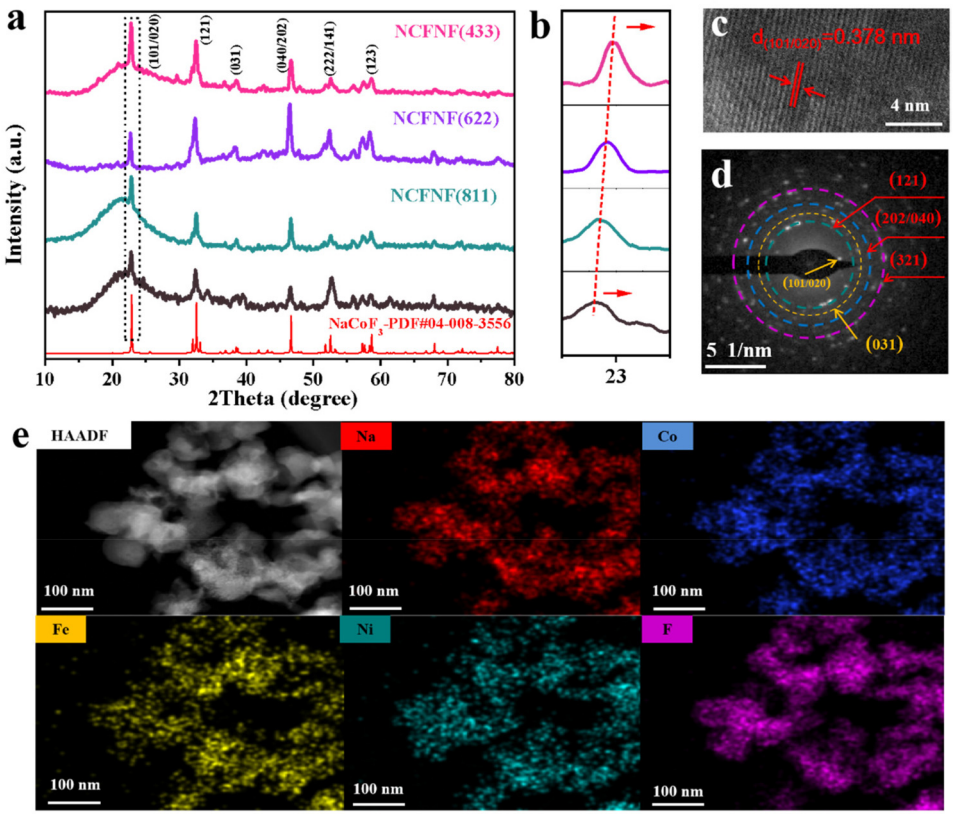

Fig. 1 (a and b) XRD patterns of $NaCo_{1-2x}Fe_xNi_xF_3$; (c) TEM image of NCFNF(433); (d) SAED pattern of NCFNF(433); (e) EDX elemental mapping for NCFNF(433).

to the perovskite fluorides. Therefore, the physicochemical properties, crystal disorder, and structure of the local atomic environment of the BF_6 octahedral could be effectively tuned by substituting perovskite fluorides at the B-site. The energy dispersive X-ray spectroscopy (EDS) results showed that Fe and Ni elements were present in the samples, which proved the successful substitution of both Fe and Ni into the NCF perovskites (Fig. 1e and Fig. S6a–c†). The proportions of metal ions in $NaCo_{1-2x}Fe_xNi_xF_3$ were determined by EDS and are listed in Table S1.†

X-ray photoelectron spectroscopy (XPS) was employed to study the chemical composition and electronic states of the perovskite fluoride $NaCo_{1-2x}Fe_xNi_xF_3$. As shown in Fig. 2a, the Co 2p peak was shifted towards higher binding energies and Co lost electrons with increasing the Fe and Ni contents, implying the oxidation of Co^{2+} to a higher valence state of Co^{3+} cations after substitution. Similarly, Fe also underwent similar changes, and a large number of Fe^{2+} cations were oxidized to Fe^{3+} cations (Fig. 2b).[31–34] Noticeably, with increasing the Fe content, the proportion of Fe^{3+} relative to Fe^{2+} increased. In addition, the high-resolution Ni 2p spectrum of NCFNF(433) showed that a part of the Ni^{3+} was completely converted into Ni^{2+} with the increase in Fe and Ni contents, which indicated that Ni could accept electrons from Fe and Co (Fig. 2c).[34] As reported earlier, Ni could cause a partial charge transfer between Co and Fe to change the electronic properties of the elements and to further form multivalent elements.[31]

Moreover, the charge transfer between the transition elements could be further illustrated by comparing the XPS results of NCF substituted with Fe or Ni only. As shown in Fig. S7a,† it was observed that the Co 2p peak of NCFF(73) with only Fe substitution was shifted to a lower binding energy compared to NCFNF(433), which showed that the electronic structure of Co was changed. Meanwhile, the results of the Fe 2p peak of NCFF(73) indicated the production of partial Fe^{3+} (Fig. S7b†).[34] The binding energy shift phenomenon in Co, Fe compounds has been reported in earlier studies. For example, recent reports[35,36] found that the Co 2p spectrum could be effectively tuned by introducing Fe to transfer higher charge, which was attributed to the transfer of electrons from Co to Fe. It is noteworthy that the Co 2p peak of the Ni-substituted NCNF(73) was not significantly shifted compared to the pure NCF (Fig. S7c†), as could be seen in Fig. S7c.† Because NCNF (73) was also present with a large amount of Ni^{3+}, this indicated that there was no significant charge transfer between Co and Ni.

Generally, it is considered that Co^{3+} and Fe^{3+} are highly active species for the OER and can be rapidly adsorbed and reacted with active molecules during the OER, which is beneficial for the OER kinetics.[35] As a result, the electronegativity of the element changes periodically with the increase in atomic number. The order of the electronegativity of Fe, Co, and Ni was: Ni > Co > Fe.[31,34] The electronegativity of the metal element becomes larger when the metal element is more active, and therefore possesses a stronger capability to

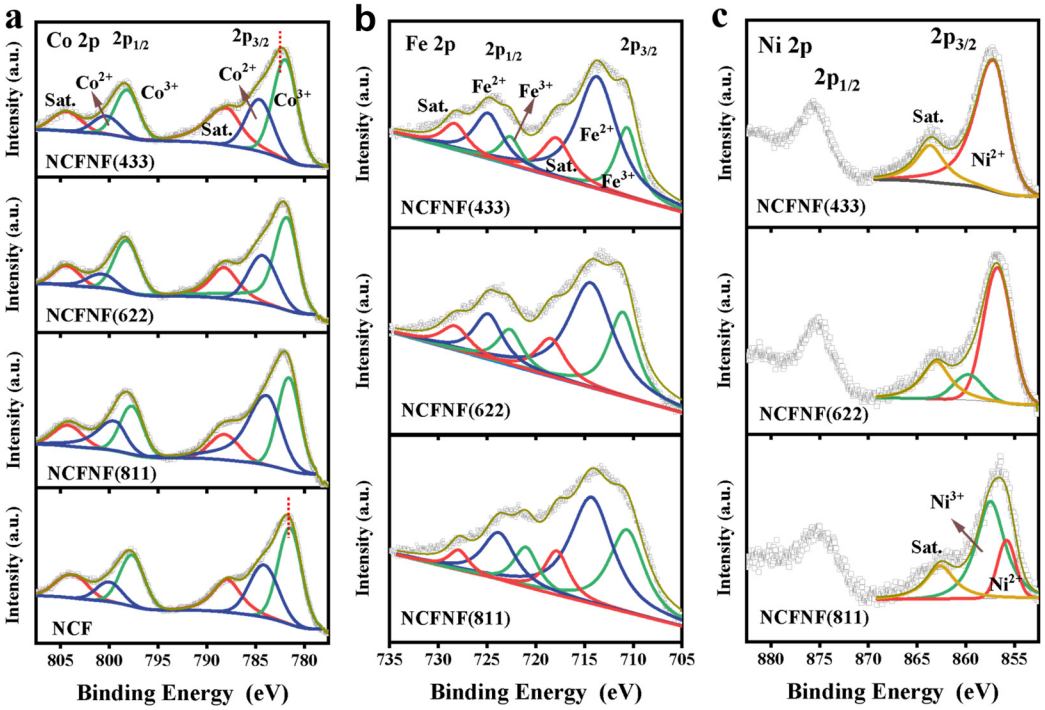

Fig. 2 (a) Co 2p XPS of NCFNF(433), NCFNF(622), NCFNF(811), and pure NCF; (b and c) Fe 2p and Ni 2p XPS of NCFNF(433), NCFNF(622), and NCFNF(811).

attract electrons. This leads to electron transfer from Co and Fe to part of Ni, thereby increasing the electron density around $NaCo_{1-2x}Fe_xNi_xF_3$, resulting in the production of Ni^{2+} species.[28,31]

To further illustrate the effect of Fe and Ni cations on the charge state and chemical bonding of the NCFNF(433) samples, synchrotron radiation X-ray absorption fine structure (XAFS) characterizations was performed. The Co K-edge oscillation curves of both Fe and Ni partially substituted NCFNF (433) were significantly different from that of the $Co(OH)_2$ precursor, but exhibited almost the same curves as CoF_3 for the counterparts (Fig. S8a†).[36,37] At the same time, the Co K-edge X-ray absorption near-edge spectra (XANES) of NCFNF(433) are shown in Fig. 3a and Fig. S8b.† After the introduction of Fe and Ni in the NCFNF(433) systems, the valence state of Co was mainly present as Co^{3+}, which was consistent with the XPS results and was confirmed by the XANES result being almost the same as CoF_3 (Fig. 3a and Fig. S8b†). In addition, the Fourier transforms (FTs) of the NCFNF(433) samples presented main peaks at about 1.53 Å, corresponding to the Co–F coordination (Fig. 3b).[38]

XANES and extended X-ray absorption fine structure (EXAFS) measurements were performed to further investigate the valence state and the coordination environment of the Fe species. As revealed by the XANES spectra at the Fe K-edge (Fig. 3c), the absorption edge of NCFNF(433) was located between FeF_2 and FeF_3, indicating the positive valence of Fe in NCFNF(433) was in the range of +2 to +3, which was in agreement with the tested XPS results.[38,39] The obtained results confirmed that Fe and Ni were successfully introduced to substitute partial Co in the lattice of NCF, and the valences of these metal ions were correspondingly changed, which is promising for achieving superior electrocatalytic activity.

The OER performance tests of our prepared perovskite fluorides were conducted on a glassy carbon electrode in 1 M KOH solution. For comparison, the electrocatalytic properties of commercial RuO_2 were tested under the same conditions. As shown in Fig. 4a, the OER polarization curves demonstrated that NCFNF(433) possessed the optimal catalytic activity among all the catalysts tested. The overpotential at a 10 mA cm^{-2} current density for NCFNF(433) was 265 mV, which was much lower than that of NCFNF(622) (278 mV), NCFNF(811) (298 mV), NCF (343 mV), and commercial RuO_2 (310 mV). In addition, in order to further reveal the intrinsic catalytic activity, the calculated turnover frequency (TOF) was investigated, and the calculated TOF values are shown in Fig. 4b.

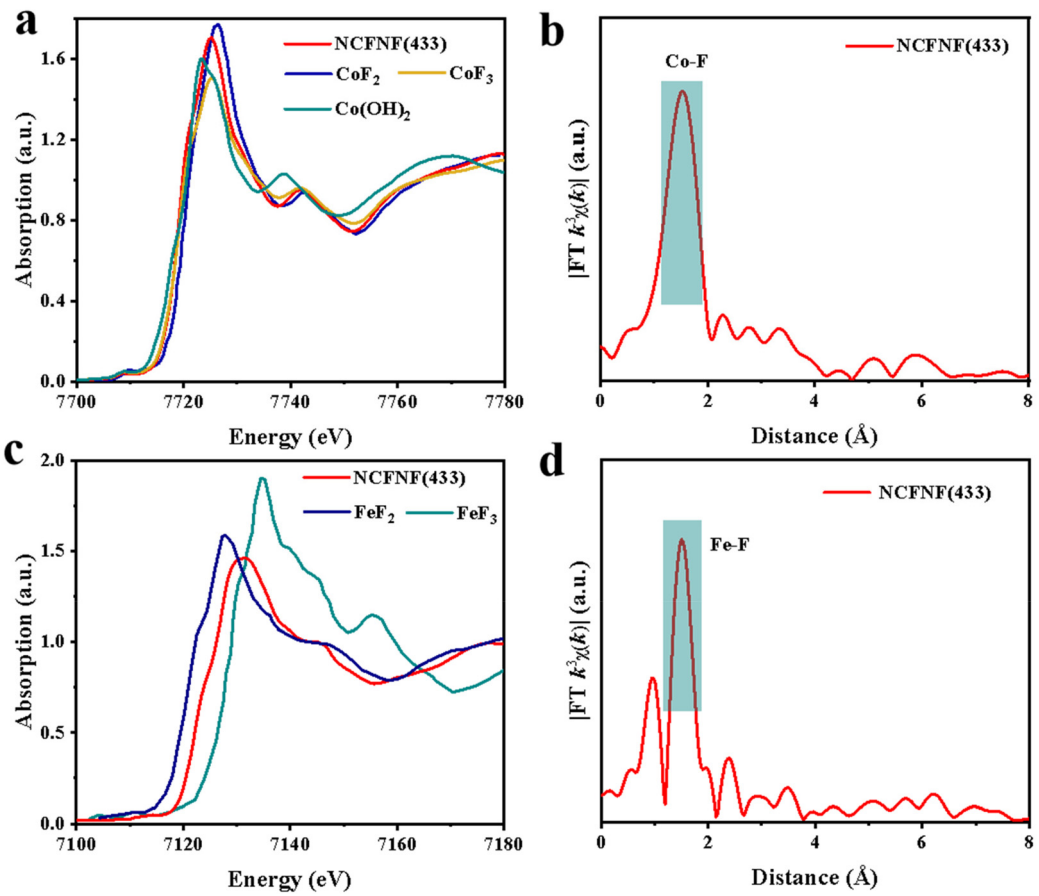

Fig. 3 (a) Co K-edge XANES of NCFNF(433), CoF_2, CoF_3, $Co(OH)_2$; (b) Fourier transforms curves of the NCFNF(433) samples; (c) Fe K-edge XANES of NCFNF(433), FeF_2, FeF_3; (d) Fourier transforms curves of the NCFNF(433) samples.

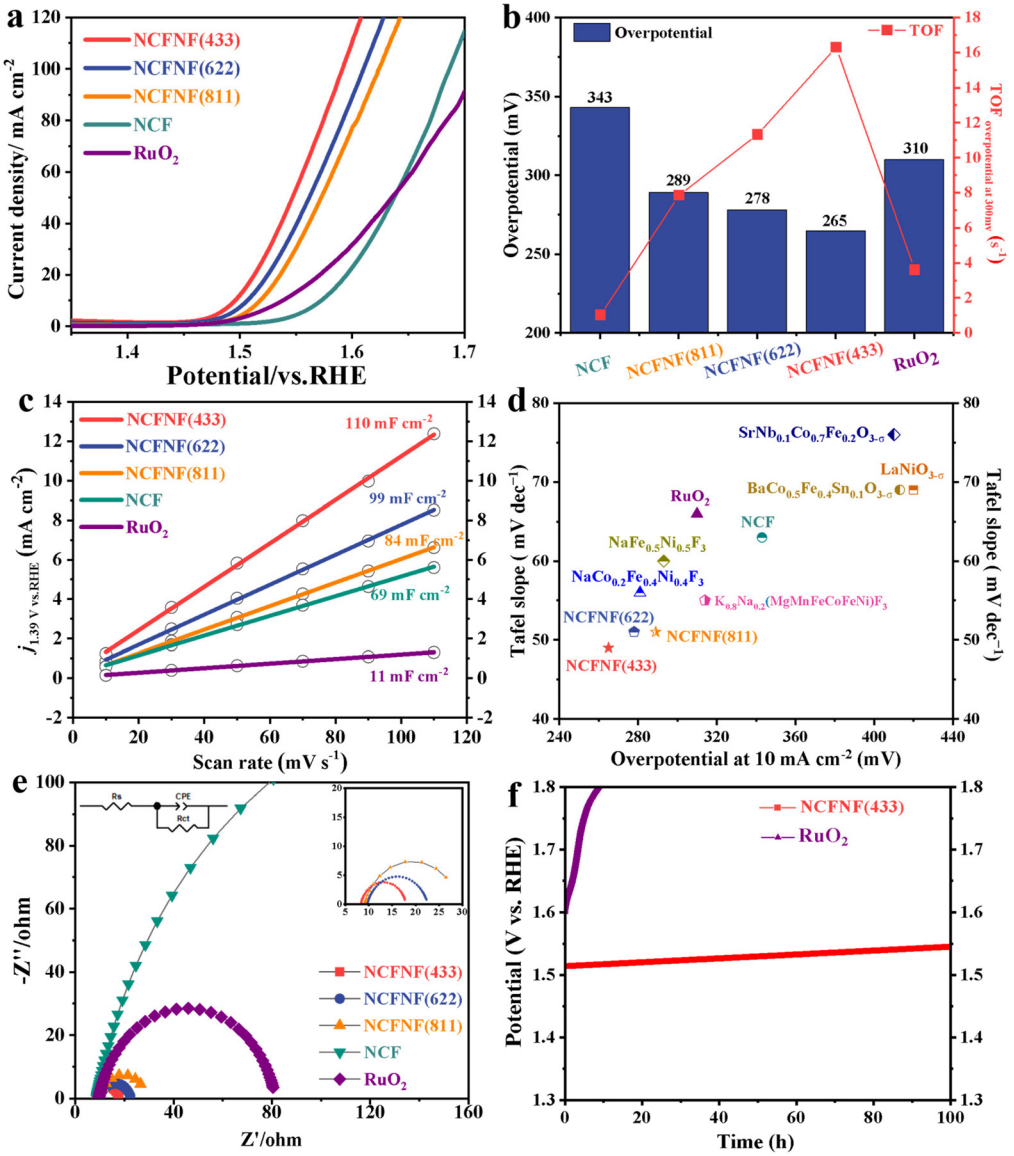

Fig. 4 Electrochemical OER performance: (a) OER polarization curves of the fluoride perovskite series samples and RuO_2; (b) comparison of the overpotentials for the catalysts at 10 mA cm^{-2} in alkaline media and the TOF at an overpotential of 300 mV; (c) charging current density differences ($j = (j_+ - j_-)/2$) at 1.39 V *vs.* RHE plotted against scan rates for the fluoride perovskite series samples and RuO_2, respectively; (d) Tafel plots for $NaCo_{1-2x}Fe_xNi_xF_3$ and the recently reported OER catalysts; (e) Nyquist plots of the catalysts in 1 M KOH at 1.524 V (*vs.* RHE) and the corresponding equivalent circuit; (f) chronopotentiometric measurements of NCFNF(433) and the commercial RuO_2 at 10 mA cm^{-2}.

NCFNF(433) displayed the highest TOF value, which was four times higher than that of RuO_2, indicating its high intrinsic electrocatalytic activity.[40] Furthermore, by normalizing the current density to the mass of the catalyst, the mass activity of NCFNF(433) was significantly increased compared with that of RuO_2 (Fig. S9†). These results indicated that the simultaneous substitution of Fe and Ni atoms could contribute to the excellent OER performance. To support this viewpoint, OER activity tests of the samples with only Fe substitution or Ni substitution were conducted (Fig. S10†). The results showed that NCFNF(433) possessed a more optimal OER activity than that of both NCFF(73) and NCNF(73) and commercial RuO_2, implying the specific synergistic effects of Fe and Ni dual-substitution.[27,39,41]

To evidence the origin of the activity for the prepared catalyst, the ECSA was determined by measuring the capacitive current associated with double-layer charging from the scan-rate dependence of the CVs (Fig. S11–S17†).[42,43] The capacitance currents shown in Fig. 4c were obtained from the corresponding CV curves. The double-layer capacitance (C_{dl}) of NCFNF(433) was calculated to be 110 mF cm^{-2}, which was about 10 times higher than that of RuO_2 (11 mF cm^{-2}). An analogous feature was also found in the specific activities normalized by the ECSA (Table S2†). This means that NCFNF(433)

has more electrocatalytically active sites for efficient OER.[43] The Tafel slopes were further calculated (Fig. 4d). The lowest Tafel slope was obtained for NCFNF(433) (49 mV dec^{-1}), while the other catalysts showed significantly higher values, verifying the fast OER catalytic kinetics of NCFNF(433).[44] Moreover, the value of 49 mV dec^{-1} for NCFNF(433) was also superior to that of most reported perovskites, including $SrNb_{0.1}Co_{0.7}Fe_{0.2}O_{3-\delta}$ nanorods (61 mV dec^{-1}),[45] $LaNiO_{3-\delta}$ (69 mV dec^{-1}),[46] $BaCo_{0.5}Fe_{0.4}Sn_{0.1}O_{3-\delta}$ catalyst (69 mV dec^{-1}),[47] and $K_{0.8}Na_{0.2}(MgMnFeCoNi)F_3$ (55 mV dec^{-1}).[25] These results revealed that the bimetallic substitution played a crucial role in improving the OER kinetics and the inner activity. This was also verified by electrochemical impedance spectroscopy (EIS) results in Fig. 4e and Fig. S18,† in which NCFNF(433) displayed a smaller resistance and excellent charge-transfer capability compared to the other catalysts.

To test the electrochemical stability of NCFNF(433) in the OER, long-term chronopotentiometry was performed at a current density of 10 mA cm^{-2}. Herein, RuO_2 was used for comparison. As shown in Fig. 4f, RuO_2 almost lost its activity after continuous 18 h OER operation. In contrast, the overpotential for NCFNF(433) just marginally increased from 265 to 296 mV after 100 h continuous testing. In order to confirm the structural change of the metal active centres during the OER process, the NCFNF(433) samples during electrochemical catalysis were tested and analyzed *via* XPS, IR, and Raman characterization, as shown in Fig. 5 and Fig. S19.† By comparing the XPS spectra of NCFNF(433) before and after the OER reaction, the Co 2p, Fe 2p, and Ni 2p spectra of the initial NCFNF(433) showed two peaks. After electrochemical catalysis, the peaks of Co 2p, Fe 2p, and Ni 2p were shifted to lower binding energies compared to the initial NCFNF(433) (Fig. 5a–c). The spin energy differences between the two bimodal peaks after electrochemical catalysis were 14.80, 11.80, and 17.40 eV, respectively, indicating the generation of MOOH (M = Co, Fe, Ni).[26] To further verify this case, infrared spectroscopy was performed, as shown in Fig. 5d, in which narrow water peaks were observed only at 3250 cm^{-1} before the electrochemical reaction, which could be caused by the water absorption of the sample, while the –OH peaks could be observed at 3000–3600 cm^{-1} and the characteristic peak of $M–O^{2-}$ at 580 cm^{-1} after the electrochemical reaction, which further indicated the formation of MOOH (M = Co, Fe, Ni).[37,48]

Furthermore, the presence of a strongly polarized metal–F bond in the fluoride perovskite would lead to the dissociation of the M–F bond to produce a metal hydroxide phase (M–OH), which can be oxidized to a higher valence metal hydroxyl oxide (MOOH) at the catalyst surface. This conclusion could

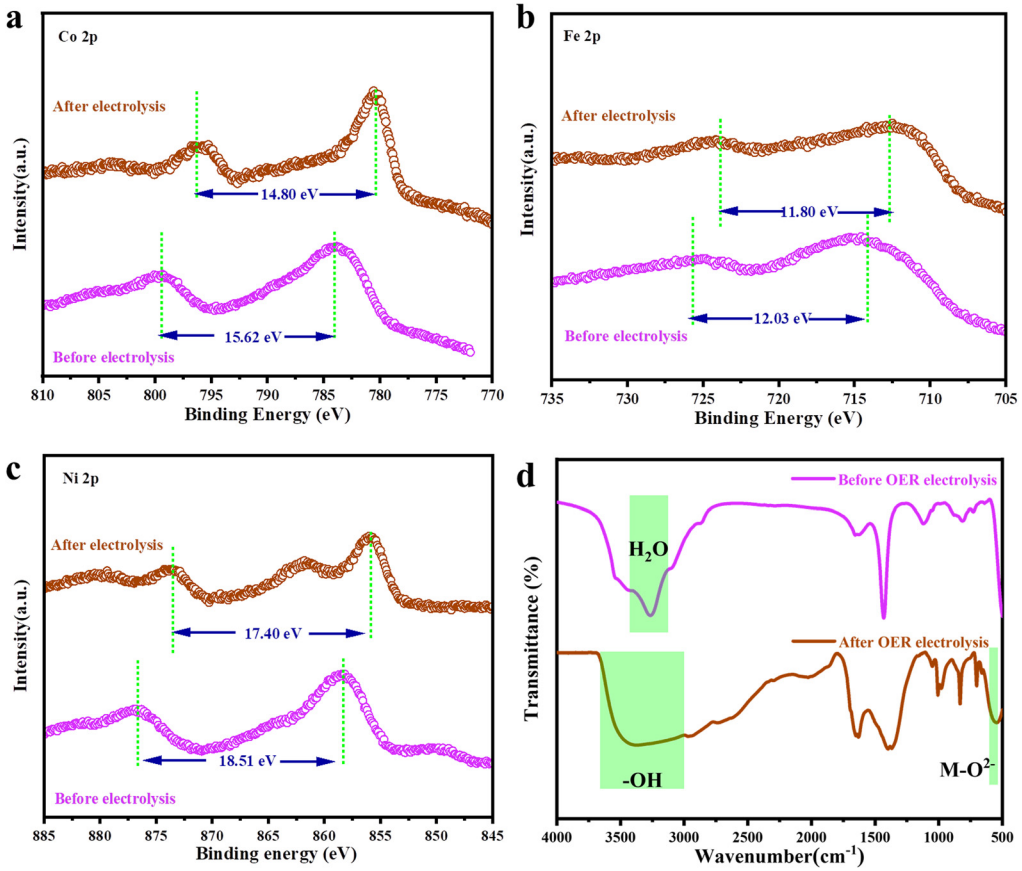

Fig. 5 (a–c) XPS results and (d) FTIR spectra of NCFNF(433) before and after the OER testing.

also be confirmed by the Raman spectra (Fig. S19†).[37,49–51] The hydroxide and hydroxyl oxide catalysts attached to the surface played a significant role in improving the OER performance.[26,52] Moreover, the more electronegative F could effectively reduce the electron density around the centre of the electrochemically active metal, which in turn promoted the OER activity. The weaker M–F bonds were more ionic, which further enhanced the OER activity.[25,28,36] It was noteworthy that surface self-reconfiguration during electrocatalytic activation has been identified in recently reported CoS_x,[53] NiFe–OH–F,[28] and $KNi_xCo_{1-x}F_3$.[26] In particular, Fan *et al.* reported the step-by-step oxidation and irreversible transformation of the amorphous electrocatalyst CoS_x to the crystalline CoOOH in the OER, and further confirmed that CoOOH is the real active species.[53] These research processes showed that the metal oxyhydroxide (MOOH) produced by surface self-reconfiguration not only contributed to the high OER catalytic activity but also to maintaining ultralong stability in the OER.

4. Conclusions

In summary, a kind of bimetallic Fe–Ni co-substituted perovskite fluoride as an advanced OER catalyst was successfully produced *via* a facile reaction process. The optimized NCFNF(433) catalyst exhibited a low overpotential of 265 mV at 10 mA cm^{-2}, a low Tafel slope of 49 mV dec^{-1}, and excellent durability for continuous 100 h operation in the OER. The improved OER performance of the NCFNF(433) catalyst was attributed to the partial substitution of Co by B-site metal species (Fe and/or Ni), resulting in a change in the electronic valence state of the B-site metal elements. The change in the electron distribution of the metal elements at the B-site produced higher valence states of Co^{3+} and Fe^{3+}, which are highly active for the OER. In addition, the part formation of amorphous MOOH (M = Co, Fe and Ni) species on the catalyst surface that act as specific active centres could obviously enhance their OER activity and cycling stability. Generally, our interesting findings provide a feasible strategy for the design of advanced perovskite-based catalysts for clean energy utilization.

Author contributions

Dr Hu Yao wrote the manuscript draft and performed experiment and data analysis. Prof. Xiaohui Guo designed and guided the project and refined the manuscript. The others contributed to the experiment testing and result discussion.

Conflicts of interest

The authors declare no competing financial interest.

Acknowledgements

This work was supported by the Key Projects of Intergovernmental International Cooperation in Key R&D Programs of the Ministry of Science and Technology of China (no. 2021YFE0115800), the National Science Funding Committee of China (no. U20A20250), the Science and Technology Committee of Shaanxi Province (grant no. 2020JZ-42), and the Project Funded by China Postdoctoral Science Foundation (no. 2022TQ0200, 2020M673630XB).

Notes and references

1 Y. Zhu, Z. He, Y. Choi, H. Chen, X. Li, B. Zhao, Y. Yu, H. Zhang, K. A. Stoerzinger, Z. Feng, Y. Chen and M. Liu, Tuning proton-coupled electron transfer by crystal orientation for efficient water oxidization on double perovskite oxides, *Nat. Commun.*, 2020, **11**, 4299, DOI: **10.1038/s41467-020-17657-9**.

2 E. Fabbri, M. Nachtegaal, T. Binninger, X. Cheng, B. J. Kim, J. Durst, F. Bozza, T. Graule, R. Schaublin, L. Wiles, M. Pertoso, N. Danilovic, K. E. Ayers and T. J. Schmidt, Dynamic surface self-reconstruction is the key of highly active perovskite nano-electrocatalysts for water splitting, *Nat. Mater.*, 2017, **16**, 925–931, DOI: **10.1038/nmat4938**.

3 X. Liang, L. Shi, Y. Liu, H. Chen, R. Si, W. Yan, Q. Zhang, G. D. Li, L. Yang and X. Zou, Activating Inert, Nonprecious Perovskites with Iridium Dopants for Efficient Oxygen Evolution Reaction under Acidic Conditions, *Angew. Chem., Int. Ed.*, 2019, **58**, 7631–7635, DOI: **10.1002/anie.201900796**.

4 J. Zhang, Z. Zhao, Z. Xia and L. Dai, A metal-free bifunctional electrocatalyst for oxygen reduction and oxygen evolution reactions, *Nat. Nanotechnol.*, 2015, **10**, 444–452, DOI: **10.1038/nnano.2015.48**.

5 X. Xu, Z. Shao and S. P. Jiang, High-Entropy Materials for Water Electrolysis, *Energy. Technol.*, 2022, **10**, 2200573, DOI: **10.1002/ente.202200573**.

6 H. Sun, X. Xu, H. Kim, W. Jung, W. Zhou and Z. Shao, Electrochemical Water Splitting: Bridging the Gaps between Fundamental Research and Industrial Applications, *Energy Environ. Mater.*, 2022, DOI: **10.1002/eem2.12441**.

7 Y. Zhao, N. Yang, H. Yao, D. Liu, L. Song, J. Zhu, S. Li, L. Gu, K. Lin and D. Wang, Stereodefined Codoping of sp-N and S Atoms in Few-Layer Graphdiyne for Oxygen Evolution Reaction, *J. Am. Chem. Soc.*, 2019, **141**, 7240–7244, DOI: **10.1021/jacs.8b13695**.

8 J. Suntivich, H. A. Gasteiger, N. Yabuuchi, H. Nakanishi, J. B. Goodenough and Y. Shao-Horn, Design principles for oxygen-reduction activity on perovskite oxide catalysts for fuel cells and metal-air batteries, *Nat. Chem.*, 2011, **3**, 546–550, DOI: **10.1038/nchem.1069**.

9 Y. Zhu, L. Zhang, B. Zhao, H. Chen, X. Liu, R. Zhao, X. Wang, J. Liu, Y. Chen and M. Liu, Improving the Activity

for Oxygen Evolution Reaction by Tailoring Oxygen Defects in Double Perovskite Oxides, *Adv. Funct. Mater.*, 2019, **29**, 1901783, DOI: **10.1002/adfm.201901783**.

10 L. Wang, K. A. Stoerzinger, L. Chang, J. Zhao, Y. Li, C. S. Tang, X. Yin, M. E. Bowden, Z. Yang, H. Guo, L. You, R. Guo, J. Wang, K. Ibrahim, J. Chen, A. Rusydi, J. Wang, S. A. Chambers and Y. Du, Tuning Bifunctional Oxygen Electrocatalysts by Changing the A-Site Rare-Earth Element in Perovskite Nickelates, *Adv. Funct. Mater.*, 2018, **28**, 1803712, DOI: **10.1002/adfm.201803712**.

11 R. Bose, V. R. Jothi, K. Karuppasamy, A. Alfantazi and S. C. Yi, High performance multicomponent bifunctional catalysts for overall water splitting, *J. Mater. Chem. A*, 2020, **8**, 13795–13805, DOI: **10.1039/d0ta02697b**.

12 L. An, J. Feng, Y. Zhang, Y.-Q. Zhao, R. Si, G.-C. Wang, F. Cheng, P. Xi and S. Sun, Controllable tuning of Fe-N nanosheets by Co substitution for enhanced oxygen evolution reaction, *Nano Energy*, 2019, **57**, 644–652, DOI: **10.1016/j.nanoen.2018.12.094**.

13 R. R. Chen, Y. Sun, S. J. H. Ong, S. Xi, Y. Du, C. Liu, O. Lev and Z. J. Xu, Antiferromagnetic Inverse Spinel Oxide $LiCoVO_4$ with Spin-Polarized Channels for Water Oxidation, *Adv. Mater.*, 2020, **32**, 1907976, DOI: **10.1002/adma.201907976**.

14 X. Lin, Y. C. Huang, Z. Hu, L. Li, J. Zhou, Q. Zhao, H. Huang, J. Sun, C. W. Pao, Y. C. Chang, H. J. Lin, C. T. Chen, C. L. Dong, J. Q. Wang and L. Zhang, 5f Covalency Synergistically Boosting Oxygen Evolution of $UCoO_4$ Catalyst, *J. Am. Chem. Soc.*, 2022, **144**, 416–423, DOI: **10.1021/jacs.1c10311**.

15 H. Liao, T. Luo, P. Tan, K. Chen, L. Lu, Y. Liu, M. Liu and J. Pan, Unveiling Role of Sulfate Ion in Nickel–Iron (oxy) Hydroxide with Enhanced Oxygen-Evolving Performance, *Adv. Funct. Mater.*, 2021, **31**, 2102772, DOI: **10.1002/adfm.202102772**.

16 M. Zhang, G. Jeerh, P. Zou, R. Lan, M. Wang, H. Wang and S. Tao, Recent development of perovskite oxide-based electrocatalysts and their applications in low to intermediate temperature electrochemical devices, *Mater. Today*, 2021, **49**, 351–377, DOI: **10.1016/j.mattod.2021.05.004**.

17 H. Jonathan, R. R. Reshma, G. Livia, K. Yu, Y. Yang and S.-H. Yang, Perovskites in catalysis and electrocatalysis, *Science*, 2017, **358**, 751–756, DOI: **10.1126/science.aam7092**.

18 X. Xu, C. Su and Z. Shao, Fundamental Understanding and Application of $Ba_{0.5}Sr_{0.5}Co_{0.8}Fe_{0.2}O_{3-\delta}$ Perovskite in Energy Storage and Conversion: Past, Present, and Future, *Energy Fuels*, 2021, **35**, 13585–13609, DOI: **10.1021/acs.energyfuels.1c02111**.

19 D. Q. Guan, J. Zhong, H. Y. Xu, Y. C. Huang, Z. W. Hu, B. Chen, Y. Zhang, M. Ni, X. M. Xu, W. Zhou and Z. P. Shao, A universal chemical-induced tensile strain tuning strategy to boost oxygen-evolving electrocatalysis on perovskite oxides, *Appl. Phys. Rev.*, 2022, **9**, 011422, DOI: **10.1063/5.0083059**.

20 C. Liu, D. Ji, H. Shi, Z. Wu, H. Huang, Z. Kang and Z. Chen, An A-site management and oxygen-deficient regulation strategy with a perovskite oxide electrocatalyst for the oxygen evolution reaction, *J. Mater. Chem. A*, 2022, **10**, 1336–1342, DOI: **10.1039/d1ta09306a**.

21 J. Sun, L. Du, B. Sun, G. Han, Y. Ma, J. Wang, H. Huo, C. Du and G. Yin, Bifunctional $LaMn_{0.3}Co_{0.7}O_3$ Perovskite Oxide Catalyst for Oxygen Reduction and Evolution Reactions: The Optimized eg Electronic Structures by Manganese Dopant, *ACS Appl. Mater. Interfaces*, 2020, **12**, 24717–24725, DOI: **10.1021/acsami.0c03983**.

22 Y. Duan, S. Sun, S. Xi, X. Ren, Y. Zhou, G. Zhang, H. Yang, Y. Du and Z. J. Xu, Tailoring the Co 3d-O 2p Covalency in $LaCoO_3$ by Fe Substitution to Promote Oxygen Evolution Reaction, *Chem. Mater.*, 2017, **29**, 10534–10541, DOI: **10.1021/acs.chemmater.7b04534**.

23 S. R. Ede, C. N. Collins, C. D. Posada, G. George, H. Wu, W. D. Ratcliff, Y. Lin, J. Wen, S. Han and Z. Luo, Intermediate $Sr_2Co_{1.5}Fe_{0.5}O_{6-\delta}$ Tetragonal Structure between Perovskite and Brownmillerite as a Model Catalyst with Layered Oxygen Deficiency for Enhanced Electrochemical Water Oxidation, *ACS Catal.*, 2021, **11**, 4327–4337, DOI: **10.1021/acscatal.1c00465**.

24 X. Liu, H. Gong, T. Wang, H. Guo, L. Song, W. Xia, B. Gao, Z. Jiang, L. Feng and J. He, Cobalt-Doped Perovskite-Type Oxide $LaMnO_3$ as Bifunctional Oxygen Catalysts for Hybrid Lithium-Oxygen Batteries, *Chem. – Asian J.*, 2018, **13**, 528–535, DOI: **10.1002/asia.201701561**.

25 T. Wang, H. Chen, Z. Yang, J. Liang and S. Dai, High-Entropy Perovskite Fluorides: A New Platform for Oxygen Evolution Catalysis, *J. Am. Chem. Soc.*, 2020, **142**, 4550–4554, DOI: **10.1021/jacs.9b12377**.

26 S. Guddehalli Chandrappa, P. Moni, D. Chen, G. Karkera, K. R. Prakasha, R. A. Caruso and A. S. Prakash, Fluoride Perovskite ($KNi_xCo_{1-x}F_3$) Oxygen-Evolution Electrocatalyst with Highly Polarized Electronic Configuration, *ACS Appl. Energy Mater.*, 2021, **4**, 13425–13430, DOI: **10.1021/acsaem.1c03103**.

27 S. Anantharaj, S. Kundu and S. Noda, "The Fe Effect": A review unveiling the critical roles of Fe in enhancing OER activity of Ni and Co based catalysts, *Nano Energy*, 2021, **80**, 105514, DOI: **10.1016/j.nanoen.2020.105514**.

28 B. Zhang, K. Jiang, H. Wang and S. Hu, Fluoride-Induced Dynamic Surface Self-Reconstruction Produces Unexpectedly Efficient Oxygen-Evolution Catalyst, *Nano Lett.*, 2019, **19**, 530–537, DOI: **10.1021/acs.nanolett.8b04466**.

29 C. Yu, Z. Wu, R. Liu, D. D. Dionysiou, K. Yang, C. Wang and H. Liu, Novel fluorinated Bi_2MoO_6 nanocrystals for efficient photocatalytic removal of water organic pollutants under different light source illumination, *Appl. Catal., B*, 2017, **209**, 1–11, DOI: **10.1016/j.apcatb.2017.02.057**.

30 Z. Shen, M. Qu, J. Shi, F. E. Oropeza, V. A. de la Peña O'Shea, G. Gorni, C. M. Tian, J. P. Hofmann, J. Cheng, J. Li and K. H. L. Zhang, Correlating the electronic structure of perovskite $La_{1-x}Sr_xCoO_3$ with activity for the oxygen evol-

ution reaction: The critical role of Co 3d hole state, *J. Energy Chem.*, 2022, **65**, 637–645, DOI: **10.1016/j.jechem.2021.06.032**.

31 Y. Sun, K. Xu, Z. Wei, H. Li, T. Zhang, X. Li, W. Cai, J. Ma, H. J. Fan and Y. Li, Strong Electronic Interaction in Dual-Cation-Incorporated $NiSe_2$ Nanosheets with Lattice Distortion for Highly Efficient Overall Water Splitting, *Adv. Mater.*, 2018, **30**, 1802121, DOI: **10.1002/adma.201802121**.

32 Z. Li, D. Zhao, C. Xu, J. Ning, Y. Zhong, Z. Zhang, Y. Wang and Y. Hu, Reduced $CoNi_2S_4$ nanosheets with enhanced conductivity for high-performance supercapacitors, *Electrochim. Acta*, 2018, **278**, 33–41, DOI: **10.1016/j.electacta.2018.05.030**.

33 W. Shi, R. Ding, Q. Xu, T. Yan, Y. Huang, C. Tan, X. Sun, P. Gao and E. Liu, Vacancy defective perovskite $Na_{0.85}Ni_{0.45}Co_{0.55}F_{3.56}$ nanocrystal anodes for advanced lithium-ion storage driven by surface conversion and insertion hybrid mechanisms, *Chem. Commun.*, 2019, **55**, 6739–6742, DOI: **10.1039/c9cc03053k**.

34 Y. Tuo, X. Wang, C. Chen, X. Feng, Z. Liu, Y. Zhou and J. Zhang, Identifying the role of Ni and Fe in Ni–Fe co-doped orthorhombic $CoSe_2$ for driving enhanced electrocatalytic activity for oxygen evolution reaction, *Electrochim. Acta*, 2020, **335**, 135682, DOI: **10.1016/j.electacta.2020.135682**.

35 S. Lee, L. Bai and X. Hu, Deciphering Iron-Dependent Activity in Oxygen Evolution Catalyzed by Nickel-Iron Layered Double Hydroxide, *Angew. Chem., Int. Ed.*, 2020, **59**, 8072–8077, DOI: **10.1002/anie.201915803**.

36 P. Chen, T. Zhou, S. Wang, N. Zhang, Y. Tong, H. Ju, W. Chu, C. Wu and Y. Xie, Dynamic Migration of Surface Fluorine Anions on Cobalt-Based Materials to Achieve Enhanced Oxygen Evolution Catalysis, *Angew. Chem., Int. Ed.*, 2018, **57**, 15471–15475, DOI: **10.1002/anie.201809220**.

37 H. Li, W. Yuan, Q. Wang, X. Cui, J. Jiang, S. Chen, L. Song and X. Guo, Two-dimensional Cobalt Oxy-hydrate Sulfide Nanosheets with Modified t_{2g} Orbital State of CoO_{6-x} Octahedron for Efficient Overall Water Splitting, *ACS Sustainable Chem. Eng.*, 2019, **7**, 17325–17334, DOI: **10.1021/acssuschemeng.9b04256**.

38 W. Zhang, P. N. Duchesne, Z.-L. Gong, S.-Q. Wu, L. Ma, Z. Jiang, S. Zhang, P. Zhang, J.-X. Mi and Y. Yang, In Situ Electrochemical XAFS Studies on an Iron Fluoride High-Capacity Cathode Material for Rechargeable Lithium Batteries, *J. Phys. Chem. C*, 2013, **117**, 11498–11505, DOI: **10.1021/jp401200u**.

39 B. J. Kim, E. Fabbri, D. F. Abbott, X. Cheng, A. H. Clark, M. Nachtegaal, M. Borlaf, I. E. Castelli, T. Graule and T. J. Schmidt, Functional Role of Fe-Doping in Co-Based Perovskite Oxide Catalysts for Oxygen Evolution Reaction, *J. Am. Chem. Soc.*, 2019, **141**, 5231–5240, DOI: **10.1021/jacs.8b12101**.

40 S. Lee, L. Bai and X. Hu, Deciphering Iron-Dependent Activity in Oxygen Evolution Catalyzed by Nickel-Iron Layered Double Hydroxide, *Angew. Chem., Int. Ed.*, 2020, **59**, 8072–8077, DOI: **10.1002/anie.201915803**.

41 J. Sun, L. Du, B. Sun, G. Han, Y. Ma, J. Wang, H. Huo, P. Zuo, C. Du and G. Yin, A bifunctional perovskite oxide catalyst: The triggered oxygen reduction/evolution electrocatalysis by moderated Mn-Ni co-doping, *J. Energy Chem.*, 2021, **54**, 217–224, DOI: **10.1016/j.jechem.2020.05.064**.

42 J. Xu, Y. Liu, J. Li, I. Amorim, B. Zhang, D. Xiong, N. Zhang, S. M. Thalluri, J. P. S. Sousa and L. Liu, Hollow cobalt phosphide octahedral pre-catalysts with exceptionally high intrinsic catalytic activity for electro-oxidation of water and methanol, *J. Mater. Chem. A*, 2018, **6**, 20646–20652, DOI: **10.1039/c8ta07958g**.

43 X. Miao, L. Zhang, L. Wu, Z. Hu, L. Shi and S. Zhou, Quadruple perovskite ruthenate as a highly efficient catalyst for acidic water oxidation, *Nat. Commun.*, 2019, **10**, 3809, DOI: **10.1038/s41467-019-11789-3**.

44 T. Wang, H. Chen, Z. Yang, J. Liang and S. Dai, High-Entropy Perovskite Fluorides: A New Platform for Oxygen Evolution Catalysis, *J. Am. Chem. Soc.*, 2020, **142**, 4550–4554, DOI: **10.1021/jacs.9b12377**.

45 Y. Zhu, W. Zhou, Y. Zhong, Y. Bu, X. Chen, Q. Zhong, M. Liu and Z. Shao, A Perovskite Nanorod as Bifunctional Electrocatalyst for Overall Water Splitting, *Adv. Energy Mater.*, 2017, **7**, 1602122, DOI: **10.1002/aenm.201602122**.

46 S. Zhou, X. Miao, X. Zhao, C. Ma, Y. Qiu, Z. Hu, J. Zhao, L. Shi and J. Zeng, Engineering electrocatalytic activity in nanosized perovskite cobaltite through surface spin-state transition, *Nat. Commun.*, 2016, **7**, 11510, DOI: **10.1038/ncomms11510**.

47 X. Xu, C. Su, W. Zhou, Y. Zhu, Y. Chen and Z. Shao, Co-doping Strategy for Developing Perovskite Oxides as Highly Efficient Electrocatalysts for Oxygen Evolution Reaction, *Adv. Sci.*, 2016, **3**, 1500187, DOI: **10.1002/advs.201500187**.

48 J. Ren, N. Jiang, K. Shang, N. Lu, J. Li and Y. Wu, Synergistic degradation of trans-ferulic acid by water falling film DBD plasma coupled with cobalt oxyhydroxide: Performance and mechanisms, *Chem. Eng. J.*, 2019, **372**, 321–331, DOI: **10.1016/j.cej.2019.04.147**.

49 M. Wen, Z. Li, R. Wang, Z. Li, X. Liu, G. Wang, G. Xie and L. Jiang, Facile electrodeposited amorphous Co–Mo–Fe electrocatalysts for oxygen evolution reaction, *Int. J. Hydrogen Energy*, 2022, **47**, 12506–12514, DOI: **10.1016/j.ijhydene.2022.02.001**.

50 L. Aguilera, Y. Leyet, A. Almeida, J. A. Moreira, J. P. de la Cruz, E. A. Milán-Garcés, R. R. Passos and L. A. Pocrifka, Electrochemical preparation of $Ni(OH)_2$/CoOOH bilayer films for application in energy storage devices, *J. Alloys Compd.*, 2021, **874**, 159858, DOI: **10.1016/j.jallcom.2021.159858**.

51 X. Zhao, Y. Liu, J. Wang, L. Qian, L. Yao, Z. Chen, Q. Cai, X. Xing and Z. Wu, Modulating the Hydrothermal Synthesis of Co_3O_4 and CoOOH Nanoparticles by H_2O_2 Concentration, *Inorg. Chem.*, 2019, **58**, 7054–7061, DOI: **10.1021/acs.inorgchem.9b00706**.

52 H. Liu, Z. Liu and L. Feng, Bonding state synergy of the NiF_2/Ni_2P hybrid with the co-existence of covalent and ionic bonds and the application of this hybrid as a robust catalyst for the energy-relevant electrooxidation of water and urea, *Nanoscale*, 2019, **11**, 16017–16025, DOI: **10.1039/c9nr05204f**.

53 K. Fan, H. Zou, Y. Lu, H. Chen, F. Li, J. Liu, L. Sun, L. Tong, M. F. Toney, M. Sui and J. Yu, Direct Observation of Structural Evolution of Metal Chalcogenide in Electrocatalytic Water Oxidation, *ACS Nano*, 2018, **12**, 12369–12379, DOI: **10.1021/acsnano.8b06312**.